# Part A

**WISHAWIN LERTNAWAPAN**

FEA Investigation

## 1. Background

Liquified Natural Gas (LNG) is an essential energy source critical to the international market. To support this large-scale industry, LNG must be stored in insulated containers due to its low boiling point of -162°C[1] before transport and distribution on specialised tanker vessels, known as LNG carriers. Inevitably, some LNG within the tanks will boil and cause pressure to build up within the containers, becoming a significant safety risk. One solution involves the installation of Gas Combustion Units (GCUs) directly onto LNG carriers to burn off excess gas that cannot be re-liquified.

The report focuses on the installation architecture of modular GCUs, specifically the design of lifting lug attachments, which provide direct contact points for loading operations onboard carriers. A stress analysis was performed below on a proposed design intended to keep the GCU stable as it is lifted while providing adequate space for the hydraulic lines and instrumentation cables that encircle the sidewalls.

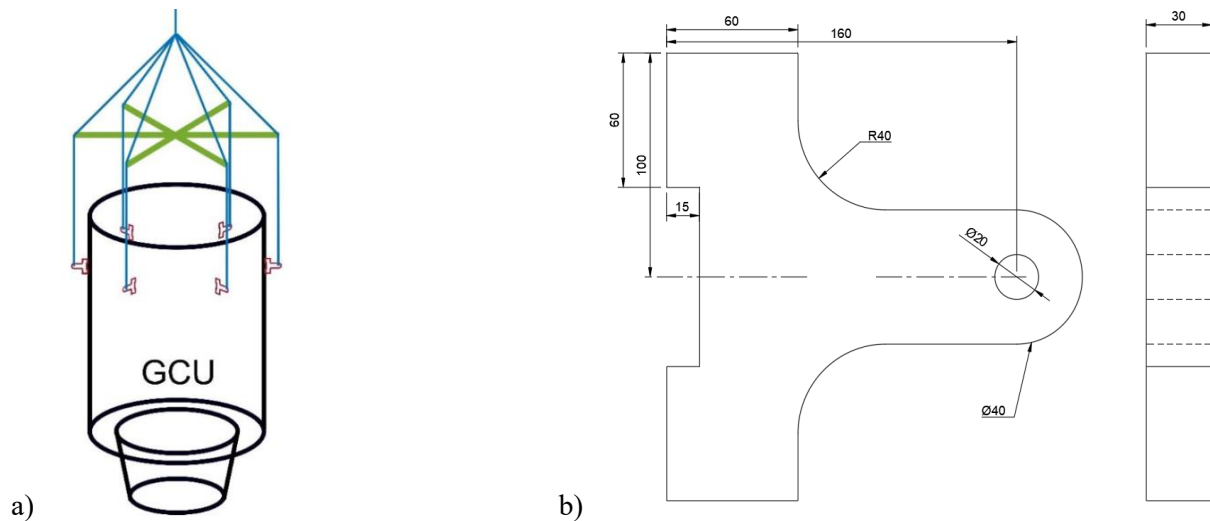A diagram of the lifting lug and arrangement is shown in Figure 1:



a)                                                                 b)

Figure 1. a) Design of the proposed lug arrangement onto the GCU module[2] (not to scale), including lifting harnesses and cables denoted in blue and green, and b) technical projection, with specific dimension values in millimetres.

The analysis aimed to ascertain the stresses experienced by the lug in typical loading conditions and conclusively justify its reliability based on safety factor considerations. The forces acting on the lug should not be sufficient to cause yielding or failure and remain at a minimum safety factor level of 5[2]. These high design requirements ensure all mechanical components included in the logistics of LNG transportation have an extremely low probability of encountering faults, as numerous historical accidents have been associated with [3].

## 2. Analysis

Component analysis was conducted using Finite Element Analysis (FEA) methods, namely the Abaqus software environment. FEA was the preferred general method to obtain numerical solutions while remaining less intensive computationally, especially in the particular case of a more complex geometry. A solid was modelled with dimensions referenced in Figure 1b), with the Von Mises stress distribution and maximum vertical tip deflection taken as outputs.

### 2.1 Material Properties

The lug is fabricated from EN 10025 – S355JR structural steel, with material properties and attributes in ambient conditions listed in Table 1[4] below. The steel is assumed to lack significant defects; chosen to be homogenous and isotropic. The pin, which is specified in section 2.2, is also considered to be manufactured out of the same steel.

Table 1. Material properties and component attributes table

| Young's Modulus $E$ / GPa | Poisson's Ratio $v$ | Yield Strength $\sigma_y$ /MPa | Ultimate Tensile Strength $\sigma_{UTS}$ /MPa | Failure Strain $\varepsilon_f$ | Density $\rho$ /kgm$^{-3}$ |
|---|---|---|---|---|---|
| 209 | 0.3 | 355 | 630 | 1.22 | 8010 |

Plastic deformation may occur within the lug if loading stresses exceed the yield strength of steel. As no ductile behaviour is explicitly stated, failure was assumed to occur at the point of ultimate tensile stress, 630 MPa, at a strain of 22%. Bilinear interpolation was then used as the most direct means of connecting the yield and failure points.

## 2.2 Loading

To most accurately represent the loading conditions experienced by the lifting shackle, a separate cylindrical component was modelled to represent the geometry and assembled in an absolute fit, where a point load is applied upwards, originating from the shackle. The magnitude of this force was identified from the mass of the GCU, which is known to be 36,000kg – distributing this mass equally across six lugs returns a load of 58,860N acting vertically on each one. By intuition, this force directly influences the ends of the modelled cylinder rather than the central point of the model. To reflect this, a point load at the centre was kinematically coupled to the end faces using a constraint.

Transferring the load causes the shackle to apply an equal force distributed over the bore surface area in the form of non-linear contact loading, where surface-to-surface contact was implemented to represent the interaction accurately. Between the contact areas of the shackle and bore, two interaction behaviours were identified: normal pressure and tangential friction using a coefficient of 0.78 (static coefficient of friction between steel-steel, ungreased)[5].
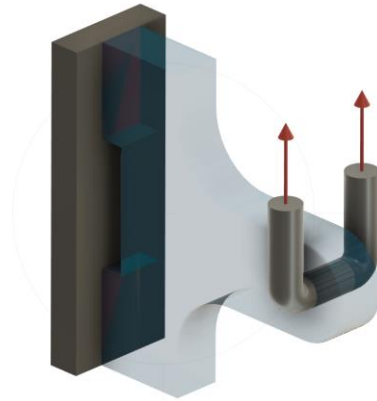


Figure 2. The loading configuration and fixed wall boundary condition are represented in red, acting through the reference point.

As this regime of loading is non-linear and performed under high loads, calculations can lead to poor convergence, a result of discontinuities between loading steps[6]. To counteract this, an intermediate step between the initial and loaded steps was analysed to ensure interaction behaviour was established between surfaces prior to total loading. Assuming the welded faces are fixed and rigid against the GCU wall, boundary conditions were applied to constrain these faces from displacement along all axes.

## 2.3 Mesh Discretisation and Sensitivity

Analysis was conducted across varying element types and mesh sizes to ensure validity in results while maintaining computational efficiency. Values for the maximum deflection $\delta$, measured at the lug tip, and Von Mises' stress $\sigma_{VM}$ were recorded for each iteration to plot a convergence trend. Note the investigated value of $\sigma_{VM}$ was only measured after neglecting the stresses at the contact point, as these inevitably experience the highest but do not contribute directly to the failure of the lug under typical beam conventions.

All computation was performed under quadratic elements to maintain high accuracy and more rapid convergence, especially in the curved geometries[6].

Reduced integration was performed where possible – by using fewer Gaussian points; stiffness tends to lower approximations to compensate for stiffness overestimation[6] in displacement-based FEA software, including Abaqus.
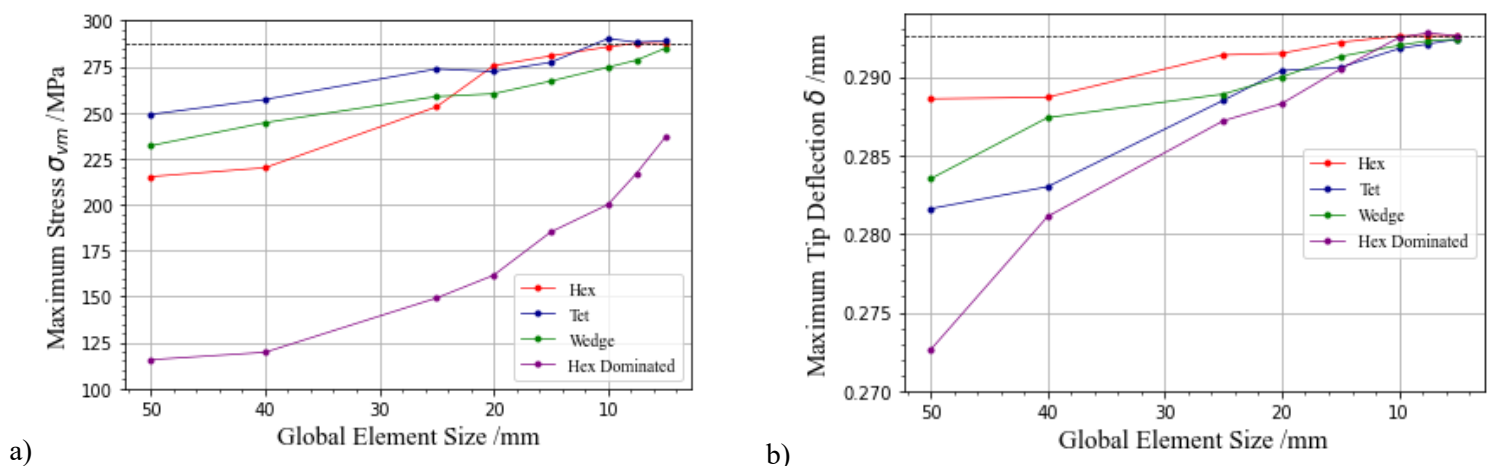


a)



b)

Figure 3. Convergence plots of maximum a) non-contact Von Mises' stress $\sigma_{VM}$, and b) vertical tip deflection $\delta$ while varying global element sizes for all elemental geometries. The black line indicates an approximation of where convergence is expected to rectify.

All meshing methods converge in deflection when element size decreases, from a minimum seed size of 5 and varied up to a length of 50mm, to remain under reasonable computational limits. Despite this, convergence is inconclusive – smaller elements are required to draw definite results. The Von Mises's stress values, conversely, do not converge convincingly due to geometrical inconsistencies at the fillet radius.

Inspection of Figure 3 shows a high degree of inaccuracies when using Hex-dominated element types. Other element types remained within 5% accuracy at element sizes below 10 and showed evident convergence. Further analysis and conclusions proceeded using a mesh of Hex C3D20R elements of seed size 5 in favour due to rapid convergence for less intensive computational times for results of similar precision to other types.

## 3. Results

The maximum non-contact Von Mises's stress was estimated to be 287.3 MPa located at the fillet region, with the maximum including the contact point found to be 453.9 MPa. A maximum vertical deflection value of 0.2926 mm situated at the tip of the lug was measured. The final model used to draw conclusions is shown in Figure 4.
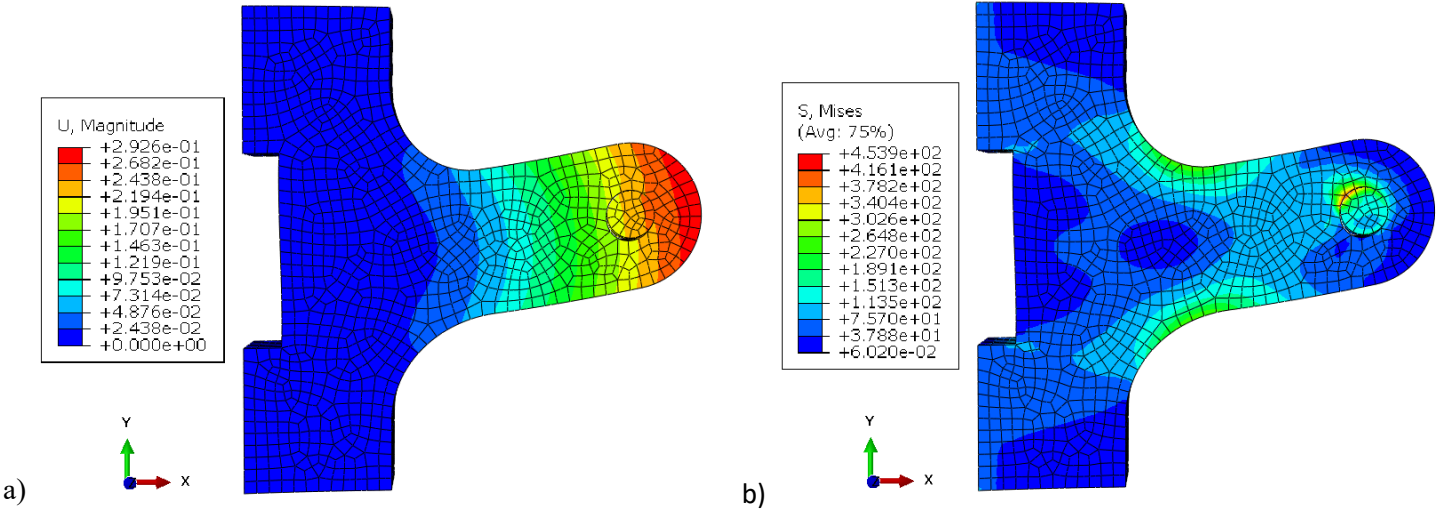


Figure 4. Deflection in mm a) and Von Mises stress in MPa b) contour models post-simulation in Abaqus, using Hex C3D20R elements with a seed size of 5mm.

Definitive interpretation of results also necessitated consideration of safety factors. Since comprehensive testing is impractical, this was conducted using rudimentary means relating theoretical strengths, $\sigma_y$ and $\sigma_{UTS}$, to the measured stress from the FEA analysis using equation 1[2].

$$Sf = \frac{\sigma_{strength}}{\sigma_{VM,max}}$$
(1)

Where $\sigma_{Strength}$ represents the theoretical strengths about each mode of failure. If $\sigma_y$ is used, the safety factor is a measure of component reliability before yield or any plastic deformation. Using $\sigma_{UTS,}$ however, will measure the ratio between intended operating loads to ductile instability failure, where the component necks and subsequently separates on a macroscopic level. Both values are summarised in Table 2.

Table 2. Safety Factor summary for both means of failure.

| Criteria | *Sf* (non-contact) | *Sf* (contact) |
|---|---|---|
| Yield Strength $\sigma_y$ | 1.236 | 0.782 |
| Ultimate Tensile Strength $\sigma_{UTS}$ | 2.193 | 1.388 |

## 4. Validation

Analytical methods were introduced to ensure the validity of the results derived earlier from FEA methods, under several assumptions made to the geometry of the beam. As the lug analysis was performed to deliver three quantities, three validation techniques were calculated to compare results to a similar standard effectively.

### 4.1 Non-Contact Stress

By approximating the behaviour of the lug as a cantilever under a predetermined state of plane stress; rigid planar sections; negligible shear contributions; entirely elastic deformations, and constant material properties – Euler-Bernoulli beam theory can be applied to approximately slender sections [7]. For this reason, the lug region between 0 < x < 60mm from the sidewall is assumed to have infinite stiffness, with an endpoint load acting from the centre of the shackle bore. Sections of the beam past this load were neglected due to their minimal contributions to the bending moment. The standard bending formula[7] is thus reduced to equation 2.

$$\sigma = \frac{6M}{th^2} \tag{2}$$

*M* represents the local bending moment, *t* is the thickness of the beam equivalent to 30 mm, and h is the vertical length of the beam cross-section, which varies by function of *x*. Solving for the maximum stress returns 210.97 MPa, at *x* = 91.2 mm from the wall, which is in justifiable proximity to the location of the high-stress elements found in FEA. The magnitude, however, is at variance by 26.6%, which, though varies significantly, is sufficient evidence to justify the model values. Considering the various assumptions made and the inability of Euler-Bernoulli theory to account for stress concentrations [8] in curved geometries culminates in a significant error; however, results remain within the same order of magnitude.

## 4.2 Vertical Deflection

Similarly, Euler-Beam theory was applied to validate the accuracy of deflection. The fillet sections were omitted. The standard formula for maximum deflection for a beam under a concentrated load [9] was used, illustrated in equation 3:

$$\delta_{\text{max}} = \frac{F\alpha^2}{6EI}(3L - \alpha) \tag{3}$$

Taking *F* as the magnitude of the load, lengths *L* and *α* measured from the assumed rigid section to the tip and the centre of the bore where the load acts, respectively, and *I* the second moment of area of a rectangular beam.
From this, a tip deflection of 0.252 mm is obtained, coinciding with a percentage difference of 13.8%. Considering the approximations made to ignore the large section of beam and type of loading, this result is highly consistent and supports the validity of the record values from FEA.

## 4.3 Contact Stresses

Elements under contact stress were approximated using bearing stress, shown in equation 4[10]. More specifically, the particular form was derived under assumptions of negligible clearance between shackle and lug bodies and elastic deformation, both of which apply directly to the system and FEA model.

$$\sigma_{\text{max}} = \frac{4F}{\pi t D}\cos\theta \tag{4}$$

Parameter *D* describes the diameter of the revolute joint and *θ* the orientation of the loading. From section 2.2, loading is specified as a point load; as such, the thickness *t* is the pressure load concentrated over the average width of a single element, producing a stress of 374.71 MPa. The resulting error is 17.5%, which provides strong evidence of the reliability of contact stress estimates.

## 5. Conclusion

Compiling the results across the investigation leads to a definitive recommendation to redesign the lug component. Analysis through FEA modelling using Abaqus packages approximates an individual lug experiences maximum stress of 287.3 MPa at the fillet point and 453.9 MPa when including the interface between the shackle and the lug. The maximum vertical deflection was found to be 0.2926 mm at the furthest distance from the GCU face. Thorough analytical techniques were used to ensure the credibility of results to a maximum difference of 26.6%. All safety factors measured below minimum industrial standards of 5[2], and in the case of the contact surface, stress is sufficient to cause plastic behaviour to be experienced.

Subsequent iterations of the lug should be altered by increasing the fillet radius and decreasing the bending moment. This can be achieved by heightening the vertical cross-section or reducing the horizontal distance from the wall from which the shackle is lifted. Additionally, a metal with an intrinsically higher yield strength may be used – such as steel with higher carbon content, or that has undergone quench and temper treatments [11].

## References

[1] Groupe International Des Importateurs De Gaz Naturel Liquefie (n.d.). LNG Information Paper No.1
[2] University of Bristol (2023). MENG30011 Applied Solid Mechanics AY2023/2024 Coursework Assessment
[3] La'o Hamutuk (2008). Appendix 4. *History of accidents in the LNG industry*
[4] World Material (2019). S355J2 Steel 1.0577 Material Properties & Equivalent.
[5] Barrett, "*Fastener Design Manual*," NASA Reference Publication 1228, 1990.
[6] Dassault Systemes Wustl.edu. (2023). ABAQUS Analysis User's Manual (v6.6).
[7] Parks, M. MIT (2004). Euler Bernoulli Beams: *Buckling, and Vibration*, 2.002 Mechanics and Materials II
[8] Hearn, E.J. (1997). Mechanics of materials. 1
[9] Captain, T. (n.d.). Academia.edu *Beam Deflection Formulae*.
[10] Spenlé, D.; Gourhant, R. (2003). Guide du calcul en mécanique *: maîtriser la performance des systèmes industriels*
[11] tec-science (2018). Quenching and tempering

# Part B
## Theory of FEA



a)                                                                                           b)
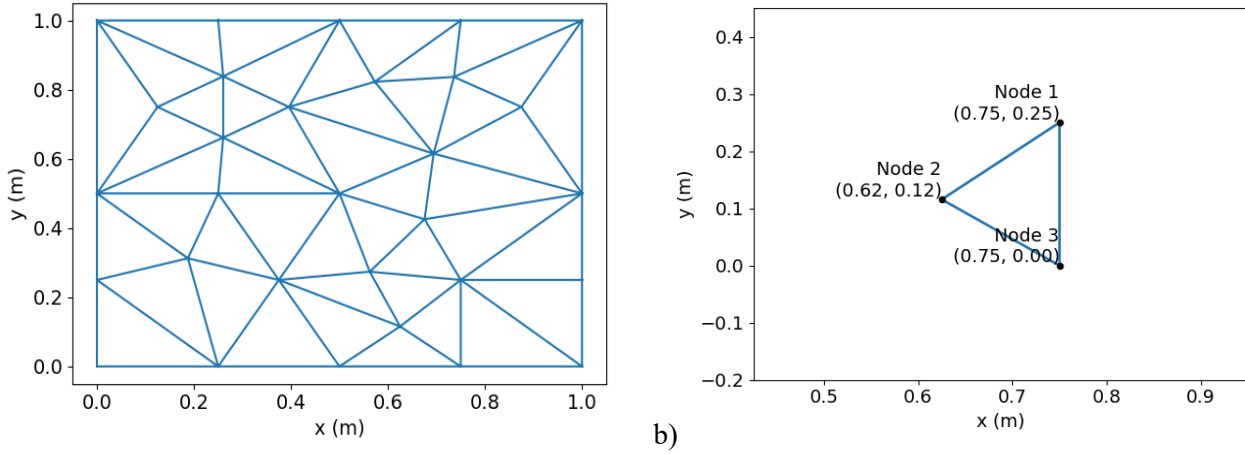
Figure 1. a) 2D Structure bounded within a finite domain, discretised into a mesh constituting of constant triangle elements. One of these elements is represented in b).

## Question 1

The mesh shown in Figure 1a is composed of 44 elements and defined by 29 nodes. Within the context of FEA, each node is capable of displacement along two dimensions, resulting in the mesh having 58 degrees of freedom.

## Question 2

An approximation for the stiffness matrix of the element shown in Figure 1b) was obtained by performing energy balance within the elements as a function of position. The element is known to be continuum and consisting of 3 nodes forming a triangle and under plane strain considerations, with the material itself specified to be isotropic, linear, and elastic.

First, by using equation 1, local displacements measured at the nodes **u** were used to define displacements **d** as a function for any given position $\vec{r}$ within the element by evaluating a Shape function, $\mathbf{N}(\vec{r})$.

$$\mathbf{d(r)} = \mathbf{N}(\vec{r})\vec{\mathbf{u}} \tag{1}$$

As the material is linear, components of $\mathbf{N}(\vec{r})$ can be interpolated individually for each node as a system of equations for $x$ and $y$ *and* then superimposed independently.

To continue, an expression for strain $\boldsymbol{\varepsilon}(\vec{r})$ was evaluated by differentiation, shown in equation 2, then substituted into a modified form of Hooke's Law in equation 5 to obtain stress $\boldsymbol{\sigma}(\vec{r})$.

$$\boldsymbol{\varepsilon}(\vec{r}) = \boldsymbol{\nabla} \mathbf{d}(\vec{r})\vec{\mathbf{u}} \tag{2}$$

$$\boldsymbol{\varepsilon}(\vec{r}) = \frac{1}{2A}\begin{bmatrix} y_2 - y_3 & 0 & y_3 - y_1 & 0 & y_1 - y_2 & 0 \\ 0 & x_3 - x_2 & 0 & x_1 - x_3 & 0 & x_2 - x_1 \\ x_3 - x_2 & y_2 - y_3 & x_1 - x_3 & y_3 - y_1 & x_2 - x_1 & y_1 - y_2 \end{bmatrix} \mathbf{u} \tag{3}$$

$$A = \frac{(x_2 y_3 - x_3 y_2) + (x_3 y_1 - x_1 y_3) + (x_1 y_2 - x_2 y_1)}{2} \tag{4}$$

$A$ quantifies the area of the triangle element, calculated using the $x$ and $y$ positions of each corresponding node.

$$\boldsymbol{\sigma}(\vec{r}) = \mathbf{D}\boldsymbol{\varepsilon}(\vec{r}) \tag{5}$$

Unlike the typical form of Hooke's Law, the material stiffness **D** depends on material property and structural information. Under 2D plane strain constraints, this takes the form

$$\mathbf{D}(\vec{r}) = \frac{E}{(1+v)(1+2v)}\begin{bmatrix} 1 - v & v & 0 \\ v & 1 - v & 0 \\ 0 & 0 & \frac{1}{2} - v \end{bmatrix} \tag{6}$$

where $v$ is Poisson's ratio, and $E$ is Young's modulus of the material.

From these, the strain energy density $U_0$ within the element was calculated from equation 7. Integrating such leads to a general formula for the total strain energy of a single element $U$; as the shape functions (and their derivatives) are constants independent of position, and the element is 2D, this simplifies to equation 11:

$$U_0(\vec{r}) = \frac{1}{2}\sigma^T(\vec{r})\varepsilon(\vec{r}) \tag{7}$$

$$U_0(\vec{r}) = \frac{1}{2}\vec{u}^T[(\nabla d(\vec{r}))^T D \nabla d(\vec{r})]\vec{u} \tag{8}$$

$$U = \iiint U_0(\vec{r})\, dV(\vec{r}) \tag{9}$$

$$U = \frac{1}{2}\vec{u}^T \iiint [(\nabla d(\vec{r}))^T D \nabla d(\vec{r}) dV(\vec{r})]\, \vec{u} \tag{10}$$

$$U = \frac{1}{2}A\vec{u}^T[(\nabla d(\vec{r}))^T D \nabla d(\vec{r})]\vec{u} \tag{11}$$

From earlier, it is known that the element behaves elastically. This leads to conservation in energy between stored strain energy $U$, and the sum of applied work done by nodal forces $W$, which is defined below (equation 12) using the linear elastic relationship between loading, $\vec{F}$ and displacement $\vec{u}$.

$$W = \frac{1}{2}\vec{F}^T\vec{u} = \frac{1}{2}\vec{u}^T K\vec{u} \tag{12}$$

Finally, by equating expressions and inspection, the stiffness matrix per unit thickness can then be represented as

$$K = \Delta[\nabla N(\vec{r})]^T D\, [\nabla N(\vec{r})] \tag{13}$$

$$K = \begin{bmatrix} y_2 - y_3 & 0 & x_3 - x_2 \\ 0 & x_3 - x_2 & y_2 - y_3 \\ y_3 - y_1 & 0 & x_1 - x_3 \\ 0 & x_1 - x_3 & y_3 - y_1 \\ y_1 - y_2 & 0 & x_2 - x_1 \\ 0 & x_2 - x_1 & y_1 - y_2 \end{bmatrix} \frac{E}{4A(1+v)(1-2v)} \begin{bmatrix} 1-v & 0 & 0 \\ 0 & 1-v & 0 \\ 0 & 0 & \frac{1}{2}-v \end{bmatrix} \begin{bmatrix} y_2 - y_3 & 0 & x_3 - x_2 \\ 0 & x_3 - x_2 & y_2 - y_3 \\ y_3 - y_1 & 0 & x_1 - x_3 \\ 0 & x_1 - x_3 & y_3 - y_1 \\ y_1 - y_2 & 0 & x_2 - x_1 \\ 0 & x_2 - x_1 & y_1 - y_2 \end{bmatrix}^T \tag{14}$$

$$K = 10^9 \begin{bmatrix} 1.193 & 0.661 & -1.830 & -0.606 & 0.636 & -0.055 \\ 0.661 & 1.299 & -0.771 & -0.559 & 0.110 & -0.740 \\ -1.830 & -0.771 & 3.812 & 0 & -1.982 & 0.771 \\ -0.606 & -0.559 & 0 & 1.165 & 0.606 & -0.606 \\ 0.636 & 0.110 & -1.982 & 0.606 & 1.346 & -0.716 \\ -0.055 & -0.740 & 0.771 & -0.606 & -0.716 & 1.346 \end{bmatrix} \text{Nm}^{-2} \tag{15}$$

**Question 3**

Calculating reaction force at Node 2 was performed using static equilibrium expression:

$$\vec{F} = K\vec{u} \tag{16}$$

Where $\vec{F}$ and $\vec{u}$ represent the vector of local forces and displacements per unit thickness at each node, respectively, and $K$ is the global stiffness matrix, note that the global stiffness matrix is indifferent to the element stiffness matrix when a single element is considered.

Given force components of $f_{1,x} = 780$kN and $f_{1,y} = 624$kN are applied locally to node 1 along the $x$ and $y$ directions, respectively, and node 2 and node 3 are restrained in both directions. The conditions alongside element stiffness matrix $K$ derived in Question 2 were substituted into equation 16 to determine the local displacements.

$$\begin{bmatrix} 780000 \\ 624000 \\ f_{2,x} \\ f_{2,y} \\ f_{3,x} \\ f_{3,y} \end{bmatrix} = 10^9 \begin{bmatrix} 1.193 & 0.661 & -1.830 & -0.606 & 0.636 & -0.055 \\ 0.661 & 1.299 & -0.771 & -0.559 & 0.110 & -0.740 \\ -1.830 & -0.771 & 3.812 & 0 & -1.982 & 0.771 \\ -0.606 & -0.559 & 0 & 1.165 & 0.606 & -0.606 \\ 0.636 & 0.110 & -1.982 & 0.606 & 1.346 & -0.716 \\ -0.055 & -0.740 & 0.771 & -0.606 & -0.716 & 1.346 \end{bmatrix} \begin{bmatrix} u_{1,x} \\ u_{1,y} \\ 0 \\ 0 \\ 0 \\ 0 \end{bmatrix} \tag{17}$$

$$\begin{bmatrix} 780000 \\ 624000 \end{bmatrix} = 10^9 \begin{bmatrix} 1.193 & 0.661 \\ 0.661 & 1.299 \end{bmatrix} \begin{bmatrix} u_{1,x} \\ u_{1,y} \end{bmatrix} \tag{18}$$

Pre-multiplication of both sides of equation 18 by the inverse of the simplified stiffness matrix according to formula 19 yields node 1 local displacements $u_{1,x} = 0.540$ mm and $u_{1,y} = 0.206$ mm.

$$\mathbf{K}^{-1} = \frac{1}{|\mathbf{K}|} \text{Adj}(\mathbf{K}) \tag{19}$$

The local displacements are then sufficient to calculate the magnitude of the components of reaction forces experienced at node 2 by substitution into equation 17 and considering rows 2 and 3:

$$\begin{bmatrix} f_{2,x} \\ f_{2,y} \end{bmatrix} = 10^9 \begin{bmatrix} -1.830 & -0.771 \\ -0.606 & -0.559 \end{bmatrix} \begin{bmatrix} 0.540 \\ 0.206 \end{bmatrix} \tag{20}$$

$$\begin{bmatrix} f_{2,x} \\ f_{2,y} \end{bmatrix} = \begin{bmatrix} -1147 \\ -4425 \end{bmatrix} \text{kNm}^{-1} \tag{21}$$

Thus, the net local reaction force was resolved using the Pythagorean theorem as components are orthogonal. At node 2, this resultant force has a magnitude of $|f_2| = 4571$ kNm$^{-1}$ is experienced, acting at an angle of 255° respective to $x$.

**Question 4**

The natural frequencies of Figure 1a require dynamic analysis and implementation of frequency-domain methods, where the following equation of motion describes behaviour for linear systems.

$$\vec{\mathbf{F}}(t) = \mathbf{M}^g \ddot{\vec{\mathbf{u}}}(t) + \mathbf{C}^g \dot{\vec{\mathbf{u}}}(t) + \mathbf{K}^g \vec{\mathbf{u}}(t) \tag{22}$$

Where $\mathbf{M}^g$, $\mathbf{C}^g$, $\mathbf{K}^g$ are matrices defining the global mass, damping, and stiffness respectively. Both the input forcing vectors $\vec{\mathbf{F}}$ and displacements $\vec{\mathbf{u}}$ (including time derivatives) are functions of time $t$. It is appropriate to assume linearity as the system comprises of elastic elements, and by considering steady-state displacements of a free vibration response will be harmonic – and more importantly – proportional to an input forcing frequency. This relationship is described in equation 23 and 24.

$$\vec{\mathbf{u}}(t) = \vec{\mathbf{U}} e^{-j\omega t} \tag{23}$$

$$\vec{\mathbf{F}}(t) = \vec{\mathbf{f}} e^{-j\omega t} \tag{24}$$

The complex exponential shorthand is used to describe the harmonic relationship present in both the input force and output displacements to a damped frequency, $\omega$. Vectors $\vec{\mathbf{U}}$ and $\vec{\mathbf{f}}$ represent the nodal mode shapes.

By substitution of the above, equation 22 can be rewritten as

$$\vec{\mathbf{f}} e^{-j\omega t} = -\omega^2 \mathbf{M}^g \vec{\mathbf{U}} e^{-j\omega t} - \omega \mathbf{C}^g \vec{\mathbf{U}} e^{-j\omega t} + \mathbf{K}^g \vec{\mathbf{U}} e^{-j\omega t} \tag{25}$$

$$\vec{\mathbf{f}} e^{-j\omega t} = [-\omega^2 \mathbf{M}^g - \omega \mathbf{C}^g + \mathbf{K}^g] \vec{\mathbf{U}} e^{-j\omega t} \tag{26}$$

$$\vec{\mathbf{f}} = [-\omega^2 \mathbf{M}^g - \omega \mathbf{C}^g + \mathbf{K}^g] \vec{\mathbf{U}} \tag{27}$$

The resulting expression maintains the linear relationship between $\vec{\mathbf{f}}$ and $\vec{\mathbf{U}}$, in similar form to static analysis, with the proportionality matrix a function of the damped frequency and containing inertial and damping components.

The solutions of $\omega$ which satisfy equation 27 represent natural damped frequencies for a system under a specific harmonic input, under which an input with an equivalent frequency will cause resonance. Given a system material damping is negligible, $\mathbf{C}$ can be ignored, and thus the solution of $\omega$ will yield the system's implicit – or free natural – frequencies $\omega = \omega_n$. In the absence of a driving force ($\vec{\mathbf{F}}(t) = 0$), the expression simplifies into an eigenvalue problem, as shown below in equation 30.

$$\vec{\mathbf{f}} = [-\omega^2 \mathbf{M}^g + \mathbf{K}^g] \vec{\mathbf{U}} \tag{28}$$

$$0 = |-\omega_n^2 \mathbf{M}^g + \mathbf{K}^g| \tag{29}$$

Pre-multiplication of the expression by the inverse global mass matrix $\mathbf{M}^{g^{-1}}$, then computing the determinant will take the general form of an eigenvalue problem (as in equation 30). The eigenvalue solutions, when solved also equal the square of values of the system's natural frequencies $\omega_n^2$.

$$|\mathbf{M}^{g^{-1}} \mathbf{K}^g - \omega_n^2 \mathbf{I}| = 0 \tag{30}$$
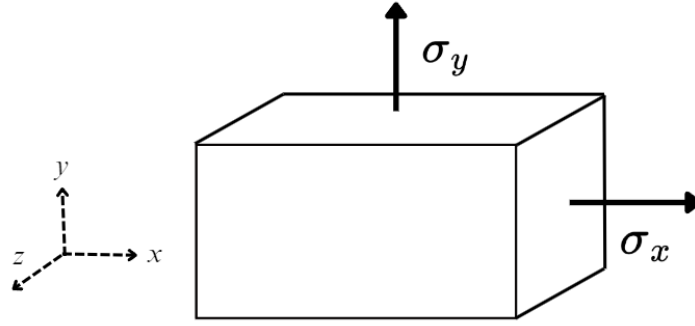
# Part C

Failure of Materials



Figure 1. Large plate structural component, loaded by normal stresses in cartesian directions $x$ and $y$. The material is given to be aluminium with properties [1] summarised in the table below.

| Yield Stress ($\sigma_y$) /MPa | Elastic Modulus ($E$) /GPa | Poisson's Ratio ($v$) | Fracture Toughness ($K_{IC}$) /MPa√m |
|---|---|---|---|
| 400 | 70 | 0.3 | 20 |

## Question 1a

In general stress states for an isotropic material, a defined stress tensor requires measurements of a minimum of three directions of strain typically arranged in a Strain Gauge Rosette [2].

From Figure 1, the only components of stress present in the diagram are influencing along $x$ and $y$. As these directions are mutually perpendicular within the same plane, and no shear stresses are present – the structure is said to be in a biaxial stress state. $\sigma_x$ and $\sigma_y$ act along principal directions, while $\sigma_z = 0$.

As these stresses are not sufficient to cause yielding, the general tensor relationships of linear elasticity [3] can be used to obtain stresses from strains:

$$\sigma_{ij} = \lambda \varepsilon_{kk} \delta_{ij} + 2\mu \varepsilon_{ij} \tag{1}$$

$$\varepsilon_{ij} = -\frac{v}{E} \sigma_{kk} \delta_{ij} + \frac{1+v}{E} \sigma_{ij} \tag{2}$$

Where $\sigma$ and $\varepsilon$ are stress and strain components respectively. $\lambda$ and $\mu$ are Lame's constants [3] given in equation 3 and 4 below

$$\lambda = \frac{Ev}{(1+v)(1-2v)} \tag{3}$$

$$\mu = \frac{E}{2(1+v)} \tag{4}$$

Expanding equation 1 using indices $i,j = 1$ and $i,j = 2$ gives the linear forms to solve for each of the principal normal stresses

$$\begin{cases} \sigma_{11} = \lambda(\varepsilon_{11} + \varepsilon_{22} + \varepsilon_{33}) + 2\mu\varepsilon_{11} \\ \sigma_{22} = \lambda(\varepsilon_{11} + \varepsilon_{22} + \varepsilon_{33}) + 2\mu\varepsilon_{22} \end{cases} \tag{5}$$

Since $\sigma_z = 0$ in a biaxial stress state, equation 2 reduces to

$$\varepsilon_{33} = -\frac{v}{E}(\sigma_{11} + \sigma_{22}) \tag{7}$$

$$\varepsilon_{33} = -\frac{\lambda}{\lambda + 2\mu}(\varepsilon_{11} + \varepsilon_{22}) \tag{8}$$

, where $\varepsilon_{33}$ can be expressed as a function of other measured principal strains. Thus, two strain measurements are required to conclusively determine both principal stresses.

## Question 1b

From the understanding of orthogonality between principal stresses, the strain gauges must also be oriented orthogonally to each other, i.e. 90° apart with the use of a T-Rosette strain gauge [4]. Under unknown principal directions, a coordinate transformation can be applied for any normal stresses [5]. However, these directions are known from Question 1a to be along the positive $x$ and $y$ axes, or $\theta = 0°$ and $\theta = 90°$ respectively.

Using these angles yields strain components from result of applied loading below:

- $\varepsilon_{11} = -0.001383$
- $\varepsilon_{22} = 0.002443$

Substituting equation 8 into 5 and rearranging provides the general form for principal stress components as function of strains in a biaxial loading conditions 9 and 10.

$$\sigma_{11} = \frac{E}{1 - v^2}(\varepsilon_{11} + v\varepsilon_{22}) \tag{9}$$

$$\sigma_{22} = \frac{E}{1 - v^2}(\varepsilon_{22} + v\varepsilon_{11}) \tag{10}$$

From these, the applied stresses along principal directions are

- $\sigma_{11} = -50.007692$ MPa
- $\sigma_{22} = 156.007$ MPa

To validate these orientations, tensor transformations were applied under the assumption of unknown principal directions. The initial results of strain gauge are not immediately accepted to be principal (as notated by $\varepsilon$`) and required manipulation using equation 11 [6].

$$\boldsymbol{\varepsilon}` = \mathbf{R_z}(\theta)\boldsymbol{\varepsilon}\mathbf{R_z^T}(\theta) \tag{11}$$

Where $\mathbf{R_z}(\theta)$ is the elemental rotation matrix clockwise about axis $z$, and $\boldsymbol{\varepsilon}$ the principal strain matrix under 2D conditions

$$\mathbf{R_z}(\theta) = \begin{bmatrix} \cos(\theta) & \sin(\theta) & 0 \\ -\sin(\theta) & \cos(\theta) & 0 \\ 0 & 0 & 1 \end{bmatrix} \qquad \boldsymbol{\varepsilon} = \begin{bmatrix} \varepsilon_{11} & 0 & 0 \\ 0 & \varepsilon_{22} & 0 \\ 0 & 0 & \varepsilon_{33} \end{bmatrix} \tag{12}$$

In index form, the following equations expand to

$$\varepsilon`_{11} = \varepsilon_{11}\cos^2(\theta) + \varepsilon_{22}\sin^2(\theta) + \varepsilon_{12}\sin2(\theta) \tag{13}$$

$$\varepsilon`_{11} = \frac{\varepsilon_{11} + \varepsilon_{22}}{2} + \frac{\varepsilon_{11} - \varepsilon_{22}}{2}\cos2(\theta) + \varepsilon_{12}\sin2(\theta) \tag{14}$$

Substituting $\theta = 0°$ and $\theta = 90°$ with the corresponding readings into $\varepsilon`_{11}$ , and solving for the principal strains will give identical results, and as expected, the in plane shear component $\varepsilon_{12}$ resolves to zero.

- $\varepsilon_{11} = -0.001383$
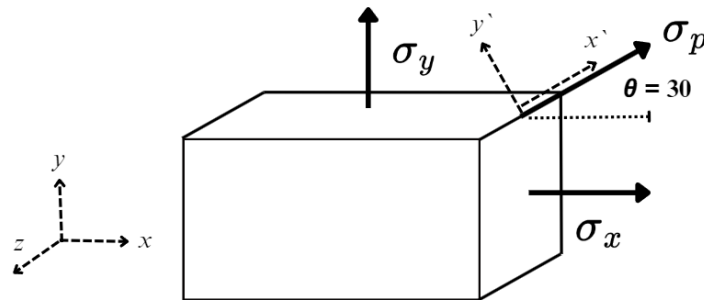- $\varepsilon_{22} = 0.002443$
- $\varepsilon_{12} = 0$

## Question 1c



Figure 2 [1]. Identical plate described previously in Figure 1, with and additional service loading stress $\sigma_p$ to be accounted. The magnitude of the stress is $|\sigma_p| \leq 400$ MPa, acting at $\theta = 30°$ from the horizontal.

There are two possible modes of failure to be considered for the specific geometry, namely ductile failure through yielding; or brittle failure via fracture. Each of these modes are independent and can be analysed separately.

**Yielding**

The two failure criteria for yielding both depend on known principal stresses. With the addition of the component of stress $\sigma_p$ acting in a distinct angle, a coordinate transformation was required.

As the component is known to be a plate, and the applied stress is acting in-plane to the other applied stresses, plane stress conditions, $\sigma_z = 0$ are likely valid and assumed in the calculation.

This simplifies the principal stress tensor (in the absence of the angled loading) to

$$\boldsymbol{\sigma} = \begin{bmatrix} \sigma_{11} & 0 & 0 \\ 0 & \sigma_{22} & 0 \\ 0 & 0 & \sigma_{33} \end{bmatrix} = \begin{bmatrix} \sigma_{11} & 0 \\ 0 & \sigma_{22} \end{bmatrix} \tag{15}$$

To combine the known tensor in equation 15 with $\sigma_p$ – described in tensor form below in equation 16 assuming uniaxial loading parallel to $x`$ in the transformed coordinate system – a stress transformation was performed [6] in similar fashion to previous equations 11 and 12.

$$\boldsymbol{\sigma}_p = \begin{bmatrix} \sigma_p & 0 \\ 0 & 0 \end{bmatrix} \tag{15}$$

Using equation 16,

$$\boldsymbol{\sigma}`_{normal} = \mathbf{R}_z(\theta)\boldsymbol{\sigma}\mathbf{R}_z^T(\theta) \tag{16}$$

Where $\mathbf{R}_z(\theta)$ is the elemental rotation matrix clockwise about axis $z$. The direct sum between equation 15 and 16 physically represent the resultant stress components in the rotated coordinate plane $x`$ and $y`$ occurring from all constituent stress components $\sigma_x, \sigma_y,$ and $\sigma_p$.

$$\boldsymbol{\sigma}` = \begin{bmatrix} \sigma`_{11} + \sigma_p & \sigma`_{12} \\ \sigma`_{12} & \sigma`_{22} \end{bmatrix} \text{ MPa} \tag{17}$$

$$\boldsymbol{\sigma}` = \begin{bmatrix} 1.496 + \sigma_p & 89.207 \\ 89.207 & 104.503 \end{bmatrix} \text{ MPa} \tag{18}$$

Under the influence of $\sigma_p$, the transformed stress tensor is no longer diagonal, with the matrix containing symmetrical shear stress components represented by $\sigma`_{12}$. Physically the result is the magnitude of both normal stresses do not assume maximum principal value.

Evaluating the principal stresses was done using by identifying the eigenvalues $\lambda$. For any Cauchy stress tensor, a principal stress exists as the eigenvalue solution which satisfies the product of the stress tensor and an arbitrary principal stress normal vector $\vec{n}$ [7]. This general relationship of such is illustrated below in equation 19

$$\lambda \begin{bmatrix} n_1 \\ n_2 \\ n_3 \end{bmatrix} = \begin{bmatrix} \sigma_{11} & \sigma_{12} & \sigma_{13} \\ \sigma_{21} & \sigma_{22} & \sigma_{23} \\ \sigma_{31} & \sigma_{32} & \sigma_{33} \end{bmatrix} \begin{bmatrix} n_1 \\ n_2 \\ n_3 \end{bmatrix} \tag{19}$$

Since plane stress conditions are assumed, the above simplifies into equation 20. By substituting the tensor $\boldsymbol{\sigma}`$ and computing the determinants in a simple eigenvalue problem, the following expression is obtained for the principal stresses in terms of applied stress, $\sigma_p$.

$$\lambda \begin{bmatrix} n_1 \\ n_2 \end{bmatrix} = \begin{bmatrix} \sigma`_{11} + \sigma_p & \sigma`_{12} \\ \sigma`_{12} & \sigma`_{22} \end{bmatrix} \begin{bmatrix} n_1 \\ n_2 \end{bmatrix} \tag{20}$$

$$\begin{vmatrix} \sigma`_{11} + \sigma_p & \sigma`_{12} \\ \sigma`_{12} & \sigma`_{22} \end{vmatrix} = 0 \tag{21}$$

$$\sigma_1, \sigma_2 = \frac{(\sigma`_{11} + \sigma_p) + \sigma`_{22}}{2} \pm \sqrt{\left(\frac{(\sigma`_{11} + \sigma_p) - \sigma`_{22}}{2}\right)^2 + \sigma`^2_{12}} \tag{22}$$

$\sigma_1, \sigma_2$ are the principal stresses in this loading arrangement as functions of $\sigma_p$.

Effective, or equivalent stress $\bar{\sigma}$ is a metric used to evaluate a component's criticality and margin to failure. In yielding, failure occurs when $\bar{\sigma} \geq \sigma_y$, where $\sigma_y$ is the tensile yield strength of a component given in Figure 1. Two commonly used criteria to quantify the equivalent stress were used below.

- **Tresca Failure Criterion**

Tresca failure criterion assumes the onset of yielding occurs when the threshold for shear stress within a material is surpassed [8]. The general expression used is provided in equation 23

$$\bar{\sigma} = \max\left[|\sigma_1 - \sigma_2|, |\sigma_1 - \sigma_3|, |\sigma_2 - \sigma_3|\right] \tag{23}$$

As the component is under plane stress, $\sigma_3 = 0$.

$$\bar{\sigma}_\text{T}(\sigma_p) = \max\left[|\sigma_2|, |\sigma_1|, |\sigma_1 - \sigma_2|\right] \tag{24}$$

- **Von Mises Failure Criterion**

In contrast, Von Mises predicts failure criticality is associated with specific distortion energy [8], where yielding occurs at the point of critical distortion energy calculated using the difference in deviatoric and hydrostatic energies.

$$\bar{\sigma}_\text{VM}(\sigma_p) = \frac{1}{\sqrt{2}}\sqrt{(\sigma_1 - \sigma_2)^2 + \sigma_2^2 + \sigma_1^2} \tag{25}$$
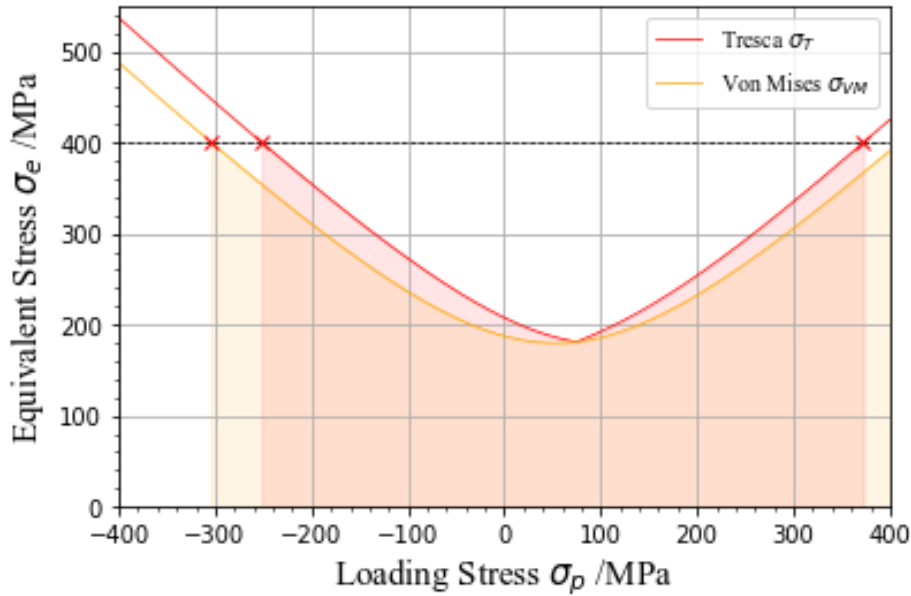


Figure 3. A plot of relationship between equivalent stress $\sigma_e$ using both yielding metrics against the applied load $|\sigma_p| \le 400$. The Von Mises criterion shows less conservative estimates for the results when compared to the Tresca criterion for the same value of $\sigma_p$. The material yield strength is also displayed along the line $\sigma_y = 400$ MPa.

From experimental data, it is known that the Tresca failure criterion is the more conservative of the two yield theories [9], thus it was used in favour when determining safety factors in the following section. However, it should be noted that the values in both cases will not differ by more than 14.4% for all stresses [9]. Here, in the range of possible loading magnitudes, failure (as denoted by the equivalent stress $\sigma_e$ exceeding 400MPa) will not occur within a specific range. This differs for each method of assessment, with a safe loading domain varying between:

- -251.852 < $\sigma_p$ < 372.773 MPa    Under Tresca Criterion
- -304.705 < $\sigma_p$    Under Von Mises Criterion

**Brittle Fracture**

The criterion used to assess the possibility of brittle fracture failure in this report relies on the principles of Linear Elastic Fracture Mechanics (LEFM). Fracture occurs when the strain energy release rate, notated as $G$ reaches a critical value $G_C$, resulting in sufficient energy to propagate a preexisting crack through its surrounding elastic stress field [10]. A generalisation is written in equation 25.

$$G = \frac{K_I^2}{E} \tag{26}$$

Griffith's theory is a particular form of the expression above, under the assumptions of a central crack propagating within an infinite plate from a result of tensile loading (referred to by Mode I opening). Due to the plate geometry, and lack of shear loading, this assumption was used to derive the form in equation 27 [11].

$$K_I = Y(a)\sigma\sqrt{\pi a} \tag{27}$$

$K_I$ is the stress intensity factor, a metric equivalent to $G$; $\sigma$ is the maximum applied tensile load in the in-plane orientation, equivalent to $\sigma_1$ as derived in equation 24; $Y$ is the dimensionless geometric correction factor which can be assumed to equal 1 within an infinite plate. The value for $a$ used is the minimum detectable crack radius, 2.5mm per investigation specifications.

Thus, brittle failure can be ascertained when $K_I \geq K_{IC}$ i.e., when the stress intensity factor exceeds aluminium's critical fracture toughness.
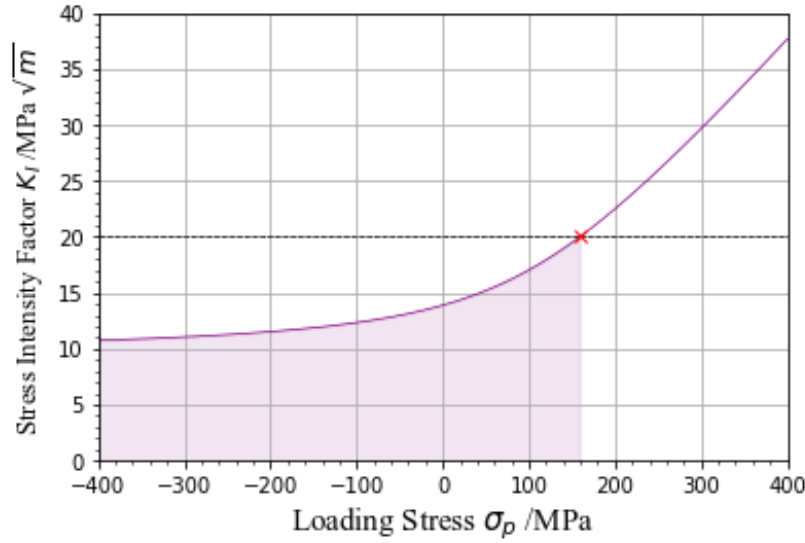


Figure 4. Graph of stress intensity factor $K_I$ as function of additional applied stress $\sigma_p$. The aluminium fracture toughness is drawn along 20MPa$\sqrt{m}$.

The relationship of stress intensity factor $K_I$ and applied stress $\sigma_p$ does not contain a lower boundary. This is intuitive, as crack growth is governed by tensile loading notated by a positive $\sigma_p$ to effectively separate the crack. The critical magnitude to cause failure through brittle fracture occurs when $\sigma_p > 158.959$ MPa.

Additionally, a safety factor was considered for both modes of failure as a means of quantifying reliability and structural integrity in design to reduce risk of failure under unintended loads or unknown parameters. For both regimes, this is defined to be the ratio between critical loading and working or equivalent loading [12] seen in equations 28, and 29.

$$Sf_{\text{yield}}(\sigma_p) = \frac{\sigma_y}{\bar{\sigma}_T(\sigma_p)} \tag{28}$$

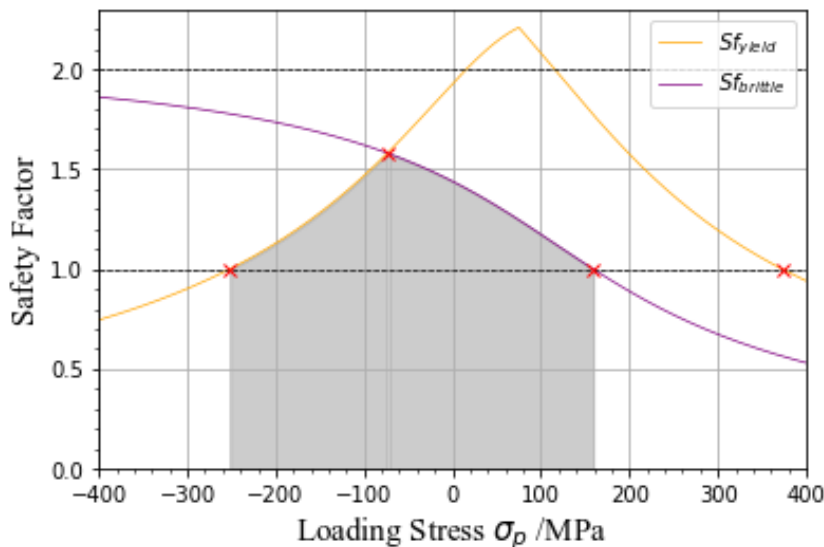$$Sf_{\text{brittle}}(\sigma_p) = \frac{K_{IC}}{K_I(\sigma_p)} \tag{29}$$



Figure 5. Graph of Safety Factors pertaining to both methods of failure. A safety factor line of 1 defines the limit, at which point the applied loading is equal to the material's intrinsic point of failure. Any domain of for which the function is below 1 is deemed unsafe and at risk of potential failure. The safe operating stress range bounded by both functions is shaded.

The safety factor plot in Figure 5 is the method used to assess the most likely failure path for the component under a specific loading magnitude. The magnitude at which each plot intersects the value of $Sf = 1$ are identical to the values listed in the previous evaluations above.

A safety factor of $Sf \geq 2$ is commonly used as the standard working limit for most structural load-bearing components including the plate in question [12]. As the majority of both functions lie underneath this line, the plate is considered unsafe and unreliable by most engineering standards. Several domains were identified in the following.

At a range of $\sigma_p \leq$ -400 MPa, failure occurs by compressive yielding.

The safe operating range lies between -251.851 $< \sigma_p <$ 158.959 MPa but additional notes can be inferred from the figure:

- Between the intervals -251.851$< \sigma_p <$ -73.273 MPa, the plate is capable of withstanding loads; however, is more prone to failure under yielding.
- Between the intervals -73.273 $< \sigma_p <$ 158.959 MPa, failure is more likely to occur consequently due to crack propagation and brittle fracture.

Past this value, where $\sigma_p \geq 400$ MPa, imminent failure is caused through means of brittle fracture.

**Crack Orientation**

To fully define potential failure mechanisms, the orientation of the central crack was also considered. Crack growth is most dominant when oriented normal to the direction of the largest principal stress [13], as this applies the greatest component of tensile force between crack faces. These orientations, known as the principal planes, can be computed by solving for the normal vector $\vec{n}$ in equation 20. The non-trivial solutions of $\vec{n}$ are the characteristic normal vectors of a scalar independent of linear transformation [14], having no components of shear stresses, i.e. principal planes. Rearranging the tensor relation in equation 20 into a standard eigenvalue problem yields the following

$$0 = (\boldsymbol{\sigma`} - \lambda \mathbf{I}_n)\vec{n} \tag{30}$$

$$0 = \begin{vmatrix} 1.496 + \sigma_p - \lambda & 89.207 \\ 89.207 & 104.503 - \lambda \end{vmatrix} \tag{31}$$

Where $\lambda = \max(\sigma_1, \sigma_2)$, acknowledging the larger of the two principal stresses defines the direction of propagation. Solving for the eigenvectors and taking the arguments produces the graph in Figure 6.
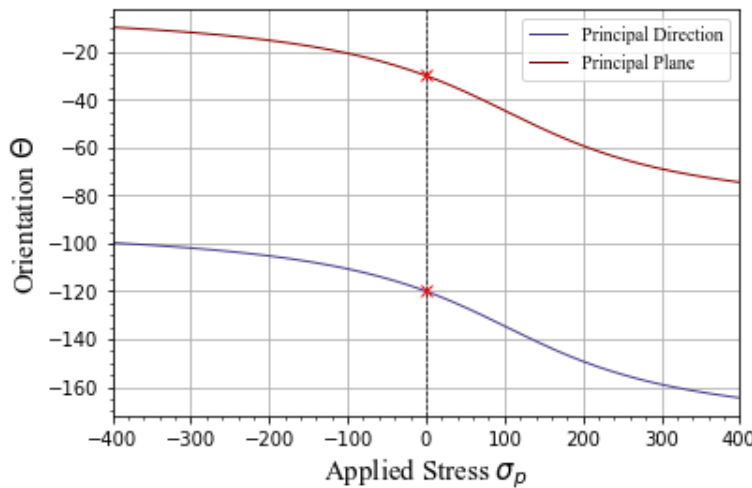


Figure 6. Plot of eigenvector, or principal directions in blue, superimposed on a translation vertically by +90° in red, denoting the principal planes on which the stresses act.

To validate these results, presuppose the system under no external applied load $\sigma_p$, marked on Figure 6 by the line at 0°. The two principal stresses are $\sigma_{11}$ and $\sigma_{22}$ from the expression derived in Question 1b. The larger, and hence the direction of maximum tensile stress is $\sigma_{22}$, acting along $y$ in the original coordinate plane or -90°. As the tensor is investigated from the rotated plane, an additional rotation of magnitude $-\theta$ ° is required to transform the angle into the appropriate reference resulting in a principal direction of -120°. Consequently, the most dangerous crack orientation is perpendicular to this at -30°.

Although crack orientation is a function of $\sigma_p$, the crack is known to fail quickest where stress intensity factor is maximised. With reference to Figure 4, it can be inferred that the worse crack orientation occurs at $\sigma_p = 400$ MPa, corresponding to an orientation of -74.5° (105.5°) measured from the positive $x`$ vector, or -104.5° (135.5°) from $x$.
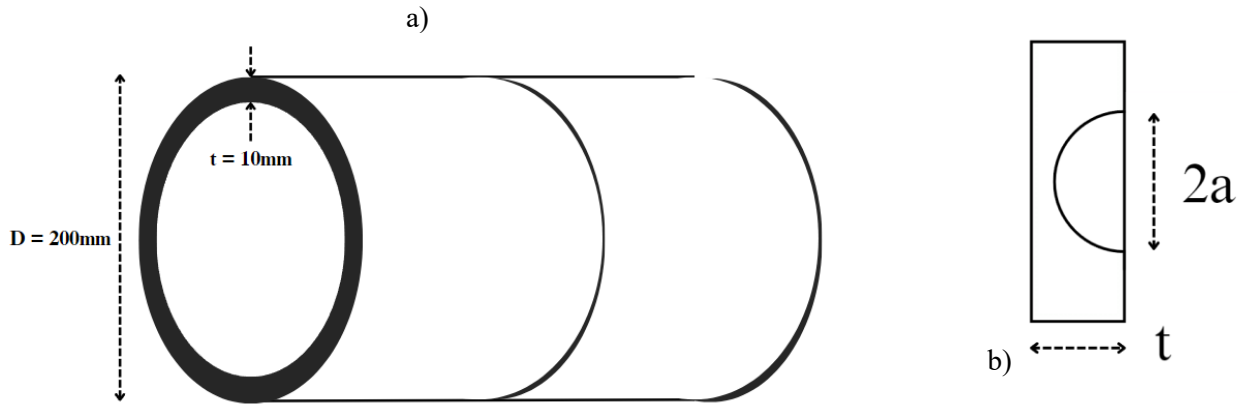
## Question 2a



Figure 7.a) Section of LNG Pipework represented as a cylindrical steel pipe [1]. Other material properties are listed in the table below. A cross sectional plane view of an arbitrary region of wall with a semi-circular crack radius a is drawn in b).

| Yield Stress ($\sigma_y$) /MPa [15] | Fracture Toughness ($K_{IC}$) /MPa√m | C / $\frac{\text{m/N}}{(\text{mPa}\sqrt{m})^m}$ | m |
|---|---|---|---|
| 1669 | 90 | $10^{-12}$ | 4 |

A separate investigation was done to assess the integrity of a section of supporting pipe network and calculate an appropriate inspection interval as a probability function. Figure 7 shows the section of pipe used for the following analysis, with a provided internal working pressure ranging between $0 < p < 40$ MPa. A possibility of valve fault should also be considered, causing a sudden short-term increase of pressure of up to 80 MPa.

To evaluate other failure forms, a small preexisting crack is assumed in the radial-circumferential plane with radius $a_p \ll t$, which expands due to loading stresses into a semi-circular crack radius $a$.

First, the failure mechanism is determined by comparing maximum loading conditions to a critical numerical value. Unlike the previous component, a pressure vessel can fail under three methods: yielding, sudden brittle fracture, and leaking.

### Yielding

As before, yield failure was located for a loading stress exceeding the yielding stress of steel, $\sigma_p \geq \sigma_y$. The elastic constitutive law was applied for a static axisymmetric component with no thermal effects and plane strain constitutive assumptions [15]. The three normal stress components in each of the cylindrical polar directions can be calculated using equations 33, 34, and 35.

$$\sigma_{rr}(p) = \frac{a^2 p}{b^2 - a^2}\left(1 - \frac{b^2}{r^2}\right) \tag{33}$$

$$\sigma_{\theta\theta}(p) = \frac{a^2 p}{b^2 - a^2}\left(1 + \frac{b^2}{r^2}\right) \tag{34}$$

$$\sigma_{zz}(p) = \frac{a^2 p}{b^2 - a^2} \tag{35}$$

Where $a$ and $b$ are the radii to the inner and outer walls respectively, $r$ the average radius, and $p$ the working pressure variable.
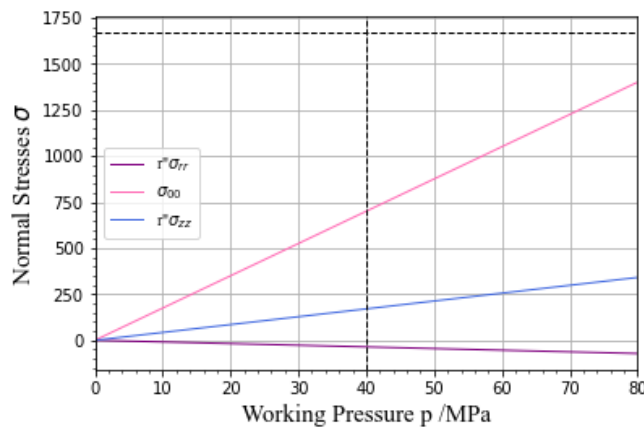


Figure 8. Plot of normal stress components in terms of working pressure $p$. The horizontal line $\sigma_y = 1669$ MPa indicates the yield limit. The range $0 < p < 40$ MPa represents the typical operating conditions, which extends to 80 MPa in the event of a fault.

From Figure 8, it was concluded that failure via yield mechanisms is highly unlikely, even when the internal pressure rises by a factor of 2 from a fault.

**Brittle Fracture**
Brittle fracture is the result of crack growth up to a critical length $a_c$ into a sudden, explosive release. This critical length may occur before the crack penetrates the vessel. Referring to equation 27, the same expression was used to calculate the stress state – with the geometry correction factor [11] in equation 36 used:

$$Y(a) = 0.728 + 0.373 \left(\frac{a}{t}\right)^2 - 0.029 \left(\frac{a}{t}\right)^2 \tag{36}$$

The value of $\sigma$ used in equation 27 must be representative of the tensile stress which is responsible for crack growth [10]. In the case of a pressure vessel with a semi-circular crack oriented in-plane of the circular face, this stress must either act along the axial or circumferential directions corresponding to $\sigma_{zz}(p)$ and $\sigma_{\theta\theta}(p)$ respectively. Assuming worse-case conditions, the larger of the two values – $\sigma_{\theta\theta}(40\text{MPa})$ – was used.

If $a$ is taken to equal $t$, the value of $Y = 1.072$ which assumes the crack has penetrated and caused failure through other means. Calculating the stress intensity factor attains $K_I = 76$ MPa$\sqrt{\text{m}}$. When comparing this value to the fracture toughness of steel used in the pipe of $K_{IC} = 90$ MPa$\sqrt{\text{m}}$, it is inferred that failure by brittle fracture is not the primary failure mechanism as penetration occurs before $a = a_c$.

**Leaking**
Leak-before-break failure in pressure vessels is identified at the point of crack penetration, $a = t$[16]. As this occurs before yielding and brittle fracture, this was concluded to be the most probable failure mechanism for the pipe.

Leaking is also characterised by incremental crack growth and fracture mechanics, however, is a governed by fatigue, which is the accumulative propagation of a crack by cyclical loading over time [17]. The mathematical relationship between crack growth $a$, and number of loading cycles $N$; or Paris Law (equation 37) was used to determine inspection intervals required, due to being the most prevalent behaviour exhibited in fatigue loading.

$$\frac{da}{dN} = C(\Delta K)^m \tag{37}$$

Which stipulates a linear log-log regime of crack growth rate for a given load ratio, known as the Paris Regime [18]. C and $m$ are empirical constants given in the properties table under Figure 7.
The number of cycles for a crack to grow from its initial length to final length can then be figured from integration.

$$N = \int_{a_i}^{t} \frac{1}{C(\Delta K)^m} da \tag{38}$$

Supposing Linear Elastic Fracture Mechanics holds true; $\Delta K$ can be substituted by equation 27, and geometric factor from equation 36, with the limits of integration between the cracks initial and final lengths. $a_i$ defines the initial crack length, varying from a minimum value $a_p$ to a maximum at failure length $t$.
Here, the minimum initial crack length from preexisting faults used was 0.1mm to remain several orders of magnitude below $t$ while providing appropriate results.

$$N = \int_{a_p}^{t} \frac{1}{C\left(Y\Delta\sigma_{\theta\theta}\sqrt{\pi a}\right)^m} da \tag{39}$$

$$N = \int_{a_i}^{0.01} \frac{1}{10^{-12}\left(0.728 + 0.373\left(\frac{a}{t}\right)^2 - 0.029\left(\frac{a}{t}\right)^2 (\sigma_{\theta\theta}(40) - \sigma_{\theta\theta}(0))\sqrt{\pi a}\right)^4} da \tag{40}$$

The parameter of $\Delta\sigma_{\theta\theta}$ defines the amplitude range of the cyclic loading stresses which can be calculated from the difference between maximum and minimum stresses in operation. As valve faults are rare occurrences, and the Paris Law approximation is only valid for a fixed load ratio [18], these additional pressures are not accounted for.

For each initial crack limit, the integrand in equation 40 can be evaluated for successive values of $a_i$. The resulting integrand represents the average number of loading cycles required to propagate the crack from $a_i$ to $t$. A numerical method was used to compute the integral, with the resulting plot highlighted in Figure 9.
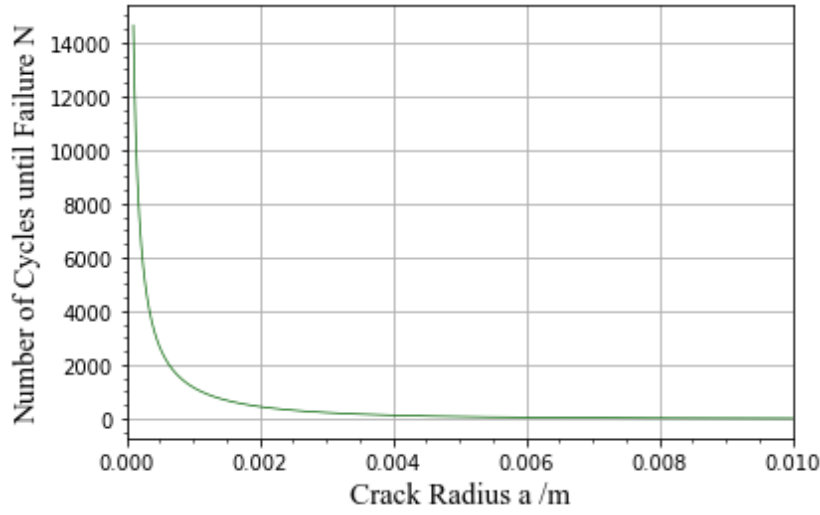
Figure 9. Number of cycles to failure from an initial crack length $a_i$, where $a_p < a_i < t$, to reach critical failure length $t$.

**Probability**

Under linear fracture mechanics, an initial preexisting crack due to surface flaw propagates in three phases. Initially, the crack is microscopic and grows due to fatigue by non-continuum mechanisms and is undetectable by conventional NDT methods. As the crack expands into the Paris Regime where leak-before-break failure is assumed to occur, an interval exists for the range of detectable crack dimensions and the critical length $a = t$. Past this, the crack transitions into a region of instability and ultimately fracture where $\Delta K_I$ exceeds $K_{IC}$ [19].

This region between detectable crack radius and leak-before-break crack radius specifies the range where inspection can take place. Intuitively, supposing failure does not occur if a crack is detected; failure relates to inspection interval by the condition of an arbitrary crack penetrating the inner radius of the vessel before inspection has taken place.

Under an additional assumption that observations are independent, the product between the number of inspections and inspection interval directly correspond to the number of cycles until failure $N(a)$,

$$N(a) = nT \tag{40}$$

where $n$ is the number of inspections within the interval $T$.

The relationship between crack radius $a$, and probability of detection of an individual crack $P_{\text{detect}}(a)$ for a crack with length equal or larger than $a$ can be described exponentially [1], stated in equation 41.

$$P_{\text{detect}}(a) = 1 - e^{-\left(\frac{a}{0.0053}\right)^4} \tag{41}$$

For a single inspection can be defined to be the probability of successful detection, as such the probability of which a component fails can be simply expressed as $1 - P_{\text{detect}}(a)$ or

$$P_{\text{failure}}(a) = e^{-\left(\frac{a}{0.0053}\right)^4} \tag{42}$$
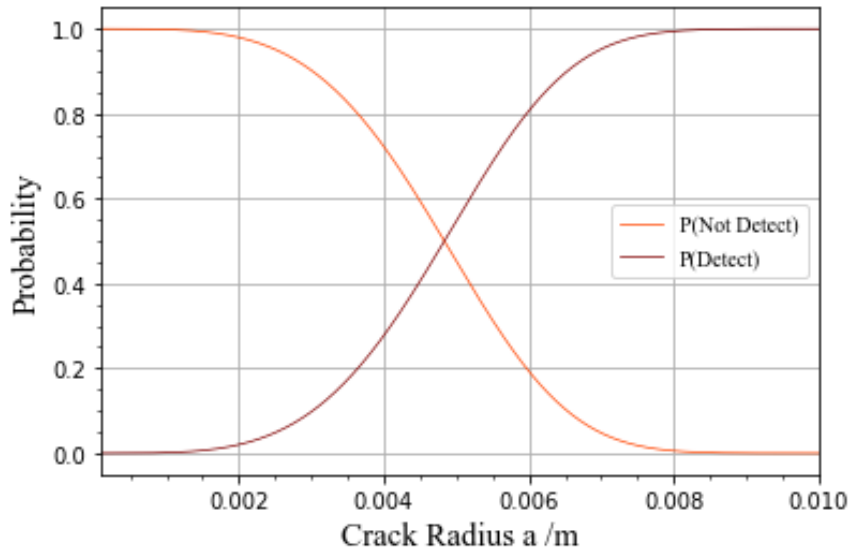


Figure 10. Probability of detection for a single random crack, drawn in red, superimposed with the Probability of not detecting – i.e., Probability of failure, drawn in orange.

Figure 10 plots the two probability functions which describe the behavior for a distinct crack, varying between the minimum detectable crack length $a_i$, up to $t$. Failure occurs as result of any crack across the component not being detected prior to inspection; and where the number of cycles remaining in the inspection period is greater than the number of cycles required to propagate the crack past critical radius. Thus the probability of failure increases as function of crack radius, up to a value of certainty when $a = t$, in which a physical interpretation is such that the probability of failure is defined as the the probability of not successfully detecting a crack of length equal or greater than which is able to expand to cause failure prior to an inspection . Since $N$ and $P_{failure}$ are functions of $a$, both can be directly associated.
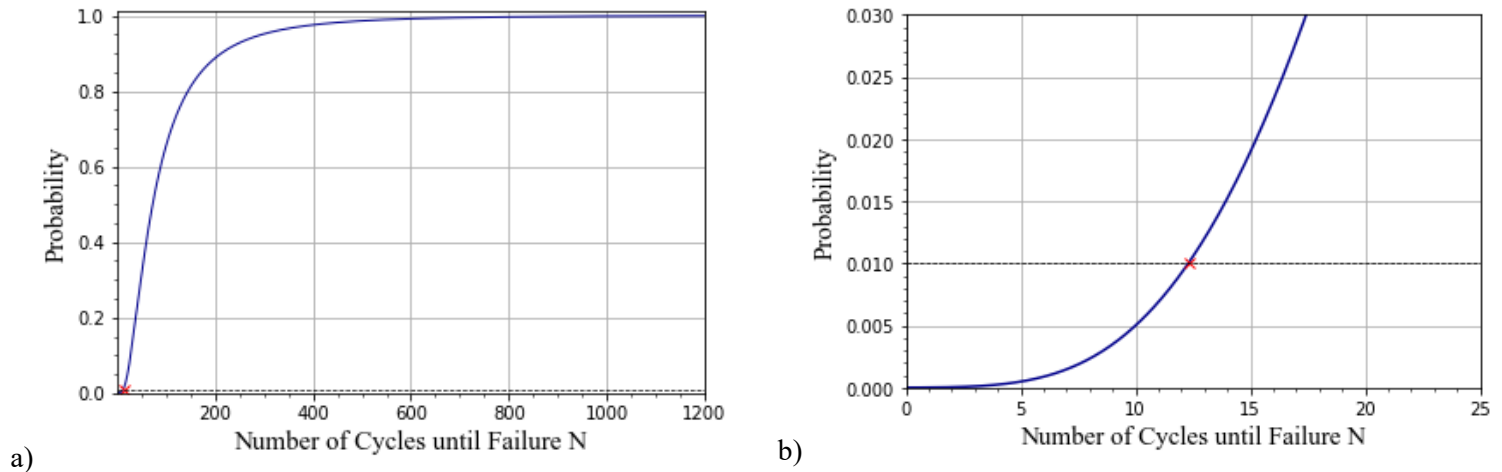


a)  b)

Figure 11. Probability of failure correlated to the function of Number of loading cycles a), using a range of crack length $0.0001 \leq a \leq 0.001$. A second adjusted view closer to the origin in the $0 < N < 25$ domain shows the intersection at 0.01 probability.

The function above in Figure 11a) illustrates the relationship of failure probability at a given number of cycles passed using the mentioned assumptions. Computing the number of cycles at 99% probability of failure is $N = 572.434$ cycles Per equation 40, the number of loading cycles $N$ is directly proportional to the interval of inspection. As only one inspection is necessary to identify a crack for a given interval, $n = 1$. Thus, the number of cycles is equivalent to the interval $T$, which establishes the relationship between $P_{failure}$, and interval of inspection $T$.

**Question 2b**
Using Figure 11b), a probability of failure 0.01 corresponds to a value of $N = 12.281$ cycles. Physically, this represents that an independent inspection is required for a minimum of every 12 loading cycles that passes to ensure probability of structural failure remains under 1%. More accurately, this number would be marginally lower to account for the incidences of increased loading due to valve faults.

**References:**

[1] University of Bristol (2023). MENG30011 Applied Solid Mechanics AY2023/2024 Coursework Assessment

[2] Micro-Measurements TN-515 (n.d.) Vishay Precision Group: Strain Gage Rosettes — *Selection, Application, and Data Reduction*

[3] Velichko A. (2023) MENG3011 Applied Solid Mechanics – Failure of Materials 5.3 *Tensor Linear Elasticity*

[4] Micro-Measurements Tech Note TN-505 (n.d.) Strain Gage Selection — *Criteria, Procedures, Recommendations*

[5] Truman C. E. (2003) An Introduction to Tensor Elasticity

[6] Kibble, T.W.B. and Berkshire, F.H. (2004). Classical Mechanics. World Scientific Publishing Company.

[7] Geotechnical Engineering. (2023). UCLA Soil Mechanics 2.3 *Principal Stresses, Eigenvalues, and Stress Paths*

[8] TU Wien.ac.at (2014). 2.3.2 *Yield Criteria*

[9] Christensen R. M. (2019).FailureCriteria Stanford Aeronautics and Astronautics Dept. *Von Mises Criterion & Tresca Criterion*

[10] Burchell, T.D. (1999). *Carbon Materials for Advanced Technologies*. Burlington: Elsevier Science

[11] Wang, C. H. (1996) Mechanics DSTO Aeronautical and Maritime Research Laboratory, *Introduction to Fracture Mechanics*

[12] Anup Kumar Dey (2020). What is Piping *Factor of Safety: Definition, Equation, Examples, Calculator*

[13] Cornell.edu. (2023). Sim Science, Cracking Dams*: Cracks Theory*

[14] MIT.edu (2013) 2.080J Structural Mechanics Recitation 2: *Stress/Strain Transformations and Mohr's Circle*

[15] University of Bristol (2022). MENG20005 Mechanics of Materials

[16] Velichko A. (2023) MENG3011 Applied Solid Mechanics – Failure of Materials 10 *Fatigue*

[17] Roylance D. (2001) MIT Cambridge, MA 02139 Fatigue

[18] Parks D. M., Anand L. (2004) MIT 2.002 Mechanics and Materials II: *Fatigue Crack Propagation*

[19] Buschow, K.H.J. (2001). Encyclopaedia of materials: *science and technology*